Scattering of $p\mu$ muonic atoms in solid hydrogen

J. Woźniak,[1,*] A. Adamczak,[2] G. A. Beer,[3] V. M. Bystritsky,[4] M. Filipowicz,[5] M. C. Fujiwara,[6] T. M. Huber,[7] O. Huot,[8] R. Jacot-Guillarmod,[8] P. Kammel,[9] S. K. Kim,[10] P. E. Knowles,[8] A. R. Kunselman,[11] G. M. Marshall,[12] F. Mulhauser,[8] A. Olin,[12] C. Petitjean,[13] T. A. Porcelli,[14] L. A. Schaller,[8] V. A. Stolupin,[4] and J. Zmeskal[15]

(TRIUMF Muonic Hydrogen Collaboration)

[1]*Faculty of Physics and Nuclear Techniques, University of Mining and Metallurgy, PL-30059 Cracow, Poland*
[2]*Institute of Nuclear Physics, PL-31342 Cracow, Poland*
[3]*University of Victoria, Victoria, Canada V8W 2Y2*
[4]*Joint Institute for Nuclear Research, Dubna 141980, Russia*
[5]*Faculty of Fuels and Energy, University of Mining and Metallurgy, PL-30059 Cracow, Poland*
[6]*Department of Physics, University of Tokyo, Tokyo 113-0033, Japan*
[7]*Gustavus Adolphus College, St. Peter, Minnesota 56082, USA*
[8]*Department of Physics, University of Fribourg, CH-1700 Fribourg, Switzerland*
[9]*University of Illinois at Urbana-Champaign, Urbana, Illinois 61801, USA*
[10]*Physics Department, Joenbuk National University, Jeonju, Jeonbuk 561-756, South Korea*
[11]*University of Wyoming Physics, Laramie, Wyoming 82071-3905, USA*
[12]*TRIUMF, Vancouver, Canada V6T 2A3*
[13]*Paul Scherrer Institute, CH-5232 Villigen, Switzerland*
[14]*Department of Physics, University of Northern British Columbia, Prince George, Canada V2N 4Z9*
[15]*Institute for Medium Energy Physics, Austrian Academy of Sciences, A-1090 Wien, Austria*

(Received 9 December 2002; revised manuscript received 18 June 2003; published 5 December 2003)

We present the results of experimental and theoretical study of the scattering of low-energy $p\mu$ atoms in solid hydrogen cooled to 3 K. Strong effects resulting from the solid state interactions have been observed in the TRIUMF experiment E742 where muons were stopped in thin frozen layers of hydrogen. The resulting emission of low-energy $p\mu$ atoms from the hydrogen layer into the adjacent vacuum was much higher than that predicted by calculations which ignored the solid nature of the hydrogen. New differential scattering cross sections have been calculated for the collisions of $p\mu$ atoms on solid hydrogen to account for its quantum crystalline nature. Analysis of the experimental data performed using such cross sections shows the important role of the coherent scattering in $p\mu$ atom diffusion. For $p\mu$ energies lower than the Bragg cutoff limit (≈ 2 meV) the elastic Bragg scattering vanishes which makes the total scattering cross section fall by several orders of magnitude, and thus the hydrogen target becomes transparent allowing the emission of cold $p\mu$ atoms to occur.

DOI: 10.1103/PhysRevA.68.062502 PACS number(s): 36.10.Dr, 39.10.+j, 61.18.Bn, 34.50.−s

I. INTRODUCTION

Negative muons stopping in hydrogen can form muonic hydrogen ($p\mu$) atoms. Although created in excited states, such atoms cascade to the ground state quickly (10^{-12} s) where their kinetic energy is of the order of several eV, much higher than thermal equilibrium energies. The muonic hydrogen atom is about 200 times smaller (m_μ/m_e scaling) than the size of ordinary electronic hydrogen. The small neutral atom can easily diffuse through the surrounding medium undergoing different types of interaction including elastic and inelastic scattering. Scattering of fast $p\mu$ atoms in hydrogen is governed by a large cross section ($\sigma_s > 10^{-19}$ cm^2) which is quite effective in slowing them down.

Only a few experiments have examined the scattering of muonic atoms on nuclei and molecules directly, although it is an important process in most muon physics phenomena such as muon catalyzed nuclear fusion (μCF) or muon nuclear capture by protons (see Refs. [1–4]). The first experiments of $p\mu + H_2$ scattering were performed in gaseous hydrogen and used the traditional diffusion method [5–8].

Much more has been done to study the scattering theoretically. Many calculations of cross sections for scattering on bare nuclei, atoms, and hydrogen molecules have been made, however, solid-state effects were not considered. The high accuracy calculations of the total cross sections for low energy scattering ($\varepsilon_{coll} < 50$ eV) for $p\mu$ and other muonic atoms on bare hydrogen nuclei (called the ''nuclear'' cross sections) were done in Ref. [9] by solving the Coulomb three-body scattering problem using the adiabatic multichannel approach. Differential cross sections for that case were calculated in Ref. [10] using phase-shift values from Ref. [9]. For collision energies lower than about $0.1-1$ eV it is necessary to account for both electron screening and the molecular structure of the target. Total and differential cross sections for this case (called the ''gas'' cross sections) are given in Refs. [11] and [12], respectively. Another possible approach to including the molecular effects for epithermal energies uses the Sachs-Teller tensor-of-mass model and can be found in Refs. [13,14].

*Electronic address: wozniak@ftj.agh.edu.pl

The scattering experiment results given in Refs. [5–8] were sometimes inconsistent not only among themselves but with theory as well (see Ref. [15] for a review). The latest and most advanced measurements in gaseous hydrogen were performed at PSI [16] where the cross sections for $p\mu$ scattering on H_2 molecules [11] were used for the analysis of the experimental data. Those measurements were not in full agreement with the theory. On the other hand, the $d\mu+D_2$ scattering measurements performed by the same collaboration [16] were in agreement.

Until now, no experimental studies concerning μ-atom scattering in solid hydrogen have been performed. Such experiments are complicated to analyze because the results for the cross section are not directly obtained but are only deduced by their effect on other results, such as time distributions or yield intensities, which themselves are often obscured by other background processes.

The development at TRIUMF of the multilayer thin frozen hydrogen film targets [17–23], which produce muonic atom beams emitted into vacuum, permitted the cross sections to be probed in another way. We have studied several isolated muon induced processes using a time-of-flight (TOF) method permitted by the frozen target geometry [23]. In particular, it was used in TRIUMF experiment E742 for the cross-section study of $d\mu+H_2$, $t\mu+H_2$ scattering, and the Ramsauer-Townsend (RT) effect which is seen for these systems at collision energies between 2 and 10 eV [24–26]. During those measurements a strong emission of low-energy $p\mu$ atoms from the hydrogen layers into adjacent vacuum was observed. The yield was much higher than expected based on calculations which ignored the solid nature of the hydrogen target. Additional experimental studies [27,28] and theoretical calculations of ''solid'' cross sections [29] have been performed in order to clarify and explain the $p\mu$ emission behavior.

This paper summarizes our findings. In Sec. II the theoretical background and new calculations of scattering cross sections in solid hydrogen are described. The experimental apparatus and the measurement method are given in Sec. III. Section IV presents the measurement results and their analysis, whereas Sec. V contains the discussion of the results and some concluding remarks.

II. SCATTERING CROSS SECTIONS

A. Scattering on bare nuclei, atoms, and molecules

Cross-section calculations for the $1S$ state $p\mu$ atom scattering on bare protons,

$$p\mu(F)+p\rightarrow p\mu(F')+p, \tag{1}$$

(where F and F' are the initial and final muonic atom spins) were begun by Gershtein [30]. He treated the process as a quantum mechanical Coulomb three-body problem. Figure 1 shows the diagram of the two isolated states of the $p\mu+p$ system with the possible transitions.

Most of the following calculations were performed in the adiabatic representation which results from expanding the wave function of a three-body system over a complete set of solutions of the two-center Coulomb problem [31], especially in the two-level approximation [32] with further modifications [33–36]. The progress in the effective potential calculation for the two–center problem permits the multichannel scattering equations to be solved even when there are a large number of closed channels [37,38]. Accurate calculations of the total cross sections performed in this multichannel approach including $p\mu+p$ scattering are presented in Ref. [9]. Reactance T matrices and phase shifts, also given in Ref. [9], for different values of the total orbital angular momentum and the total spin of the three-particle system have been used to calculate the differential cross sections [10]. Cross sections (total and differential) for collisions with energies less than ≈ 1 eV, where both electron screening and molecular binding are important (gas cross sections), are given in Refs. [11,12]. The screening effect is described there in terms of the effective screening potential, and the Fermi pseudopotential method was applied to model the chemical binding.

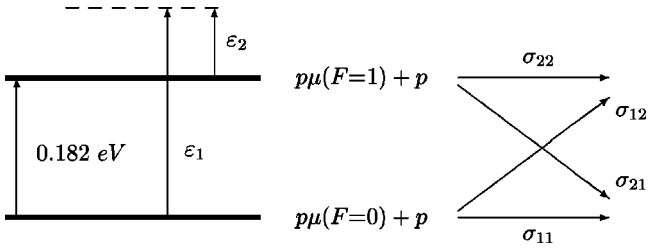

FIG. 1. Energy levels for the $p\mu+p$ system, where ε_1 and ε_2 represent the collision energies for the singlet ($F=0$) and triplet ($F=1$) states, respectively. The dashed line represents the total energy of the system. Four transitions with cross sections σ_{ik}, $i,k=1,2$ are possible due to the hyperfine splitting of the energy levels. For the scattering of $p\mu$ in the singlet state only the elastic scattering σ_{11} is possible if the collision energy ε_1 is below $E_{hfs}=0.182$ eV.

B. Cross sections for solid hydrogen

The TRIUMF experiments [17–23] have stimulated theoretical studies of μ-atom scattering in solids. Solid hydrogen at zero pressure is a quantum molecular crystal, which is characterized by a large amplitude of zero-point vibrations of the molecules. At 3 K, the vibration amplitude is $\approx 18\%$ of the nearest-neighbor distance for the H_2 molecule and 15% for the D_2 molecule [39]. Nevertheless, experiments show that quantum solids display typical crystal structures and that common crystal characteristics, such as the density of the vibrational states, are well defined. This proves that the molecular motion is correlated in such a manner that the crystalline structure is not destroyed. However, theoretical methods developed for a classical-crystal description, encounter certain problems when applied in the case of quantum crystals. Namely, the interaction potential between the hydrogen molecules has a highly repulsive anharmonic core and thus the standard lattice dynamics leads to imaginary vibration frequencies. Nevertheless, the standard dynamics can be used, after a renormalization of the interaction potential by accounting for the short-range correlations between neighboring-molecule movement.

Solid hydrogen can exist in both efficient-packing structures: face-centered cubic (fcc) and/or hexagonal close packed (hcp). Since the TRIUMF targets were formed by rapidly freezing hydrogen gas on a gold foil at 3 K and zero pressure, the solid layer has a polycrystalline fcc structure [39]. There is also experimental evidence that thin hydrogen films formed on fcc metal (e.g., gold or silver) will retain that same structure [40]. Since the fcc and hcp crystals are very similar (e.g., the molar volumes are almost the same and the first three shells of neighbors of any fixed molecule are identical in both the structures), the fcc cross sections are also a good approximation to the hcp case. The hydrogen was purified by a palladium filter at 600 K immediately prior to freezing, so the resulting solid target had a statistical distribution (1:3) of molecular rotational states $K=0$ and $K=1$. Such a mixture of rotational states is often called ''normal'' hydrogen, nH_2. The relevant lattice constant for the fcc structure at zero pressure is 0.5338 nm [39].

A method to calculate the scattering cross sections of muonic hydrogen atoms in solid hydrogen (solid cross sections) based on Van Hove's approach and using phase shifts for muonic atom scattering on bare nuclei [9,41] has been proposed by Adamczak (see Ref. [29] for details). The calculated differential cross sections include incoherent and coherent effects. The impinging muonic atom can induce inelastic reactions, both in a single molecule (rovibrational transitions or spin flip) and in the whole target (excitations or deexcitations of the lattice vibrational states). The latter are usually interpreted as creation or annihilation of phonons. It is possible to create or annihilate one or more phonons in coherent or incoherent processes, but in practice, annihilation processes are strongly suppressed in a 3-K target because few phonons exist at low temperatures.

Figure 2 presents the calculated total cross sections for $p\mu$ scattering on 3-K solid fcc hydrogen for different initial and final spin states F of the $p\mu$ atom. Also shown are some details of the total cross section for $p\mu$ atom scattering from the ground spin state $F=0$. For the sake of comparison, the doubled cross section $\sigma_{11}^{\rm nuc}$ of $p\mu(F=0)+p$ nuclear scattering is plotted. The cross sections are given for a single bound molecule. At energies greater than roughly 1 eV both the solid-state and molecular binding effects are very small and therefore the cross section for a real hydrogen target is well described by the nuclear cross section.

In Fig. 2, there is an important difference between the singlet-(σ_{11}, $F=0$) and triplet-(σ_{22}, $F=1$) state scattering. For the singlet, only the state $J=\frac{1}{2}$ of the total spin of the $p\mu+p$ system is possible. As a result, the scattering in nH_2 is almost fully coherent and thus interference effects determine the behavior of the singlet cross section at the lowest energies. Below the Bragg cutoff energy, $E_B\approx 2$ meV, elastic and phonon-creation coherent scattering is impossible and the total cross section is determined by the weak incoherent processes, which gives rapid falloff of σ_{11}. Coherent phonon annihilation is present below E_B, but its magnitude is very small at 3 K. The rotational deexcitation $K=1\rightarrow K'=0$ of a H_2 molecule gives no contribution to the cross section since this transition is strictly forbidden for $F=0$.

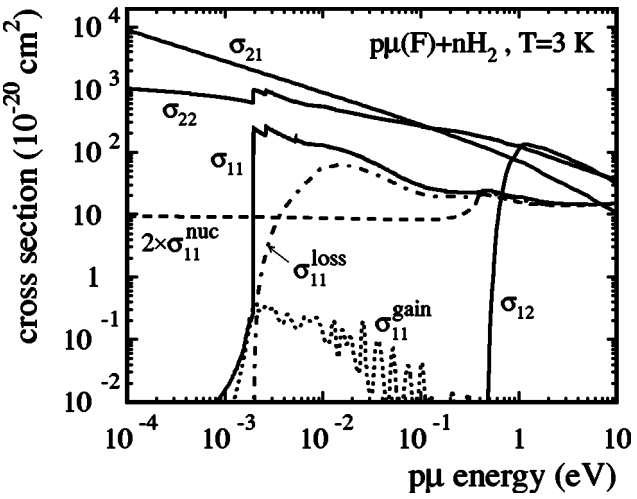

FIG. 2. Total cross sections for $p\mu(F)$ scattering in 3-K polycrystalline nH_2 with the fcc structure, for different values of the initial and final muonic atom spin, F. The dotted line represents the phonon-annihilation fraction of σ_{11} that results in $p\mu$ energy gain; the sum of contributions from phonon creation and rovibrational excitations to σ_{11}, which lead to $p\mu$ energy loss, is denoted by dash-dotted line. The doubled nuclear scattering cross section $\sigma_{11}^{\rm nuc}$ for $p\mu(F=0)+p$ is shown for comparison (dashed line). Note the Bragg cutoff energy E_B at $\varepsilon\approx 2$ meV for σ_{11}.

Scattering of the $p\mu(F=1)$ atom is possible in the two total-spin states: $J=\frac{1}{2}$ and $J=\frac{3}{2}$. The nuclear amplitudes for these two processes are very different [9] and therefore averaging the molecular scattering amplitude over spins leads to a strong incoherent component. As a result, the cross section σ_{22} in solid hydrogen has a large magnitude at $\varepsilon\rightarrow 0$, though a small falloff of its value at E_B is still present. Significant contribution to σ_{22} at lowest energies comes also from the rotational deexcitation $K=1\rightarrow K'=0$, which is possible (for $F=1$) due to the exchange of the muon between the protons during the collision process.

In Fig. 2 contributions to σ_{11} are shown from different processes. The energy region 2–10 meV is dominated by the strong elastic Bragg scattering. Phonon annihilation, denoted by the label $\sigma_{11}^{\rm gain}$, is the only mechanism of $p\mu$ acceleration. Weak incoherent elastic scattering is most important below E_B. Slowing of $p\mu$ is possible through the lattice excitations and then, at sufficient incident energy, through subsequent rotational and vibrational excitations. The rovibrational transitions may take place with simultaneous one or multiphonon creation. The curve which shows the sum of contributions from all these processes is labeled by $\sigma_{11}^{\rm loss}$. At $\varepsilon\gtrsim\omega_D$, the inelastic processes are most important and the cross section for the solid (per single molecule) approaches the corresponding one for a free H_2 molecule.

Figure 3 illustrates the small differences between Bragg scattering of $p\mu$ in the fcc and hcp polycrystalline nH_2. The Bragg cutoff energy is slightly (≈ 0.2 meV) smaller in the hcp target. Different Bragg peak patterns in the total cross sections are distinct only below a few meV. The magnitudes of the cross sections are similar in the two lattices and, therefore, the theoretical estimation of cold-$p\mu$ emission, ob-

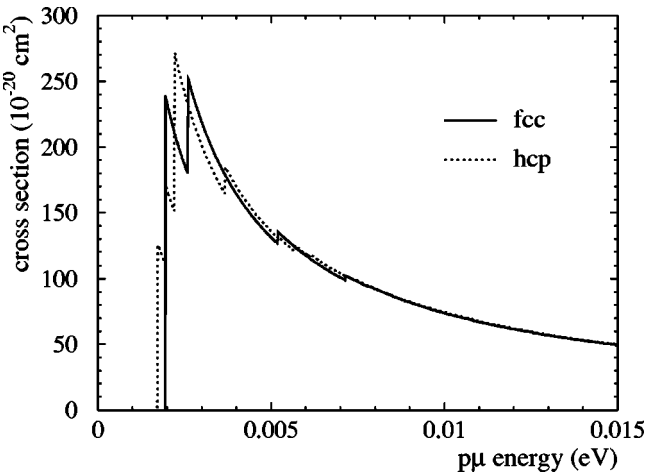

FIG. 3. Total cross section for Bragg scattering of $p\mu(F=0)$ atoms in 3-K polycrystalline nH_2 with the fcc (solid line) and hcp (dotted line) structure.

tained in this work for an fcc target, is also valid in the hcp case.

C. Slowing down of $p\mu$ atoms in solid hydrogen

The slowing down of $p\mu$ in solid hydrogen has been simulated by the Monte Carlo method using the new cross sections. The more important characteristics are shown in the following figures.

The simulations, performed with the Monte Carlo code FOW [42], represent a real experimental situation where muons were stopped and formed $p\mu$ atoms in a solid protium target of thickness 3.4 mg cm^{-2} (an experiment labeled later as No. 3 in Table IV). For this presentation only the histories of $p\mu$ resulting in the upstream emission from the hydrogen layer have been chosen.

Scatter plots on Figs. 4 and 5 illustrate the time dependence of the $p\mu$ slowing down (2376 histories ending by the emission from the hydrogen layer are shown). Each point represents the $p\mu$ energy after a scattering event at a given time. Figure 4(a) shows a sampling of all events during slowing down, whereas Fig. 4(b) shows only the final coordinates when $p\mu$ emission has occurred. One sees that the slowing down process is very fast and that after $\approx$10 ns, the $\sim$meV energy region is reached. Further decelerations of the $p\mu$ are then slower since the responsible inelastic cross sections become lower. This transient region extends to 100–200 ns when equilibrium energy is reached and $p\mu$ atom diffusion in hydrogen takes place. The equilibrium energy is established near the Bragg cutoff limit where both the phonon creation and annihilation components of σ_{11} become equal (see Fig. 2).

Figure 5 represents contributions to slowing down from separate processes for $p\mu$ in singlet and triplet states. In any experiment both $p\mu$ atomic spin states will be initially populated, however, the downward spin–flip is so fast in the solid target that, after 0.1 ns, practically all $p\mu$ atoms are in the ground spin state. Therefore, further slowing down is governed by the cross section σ_{11} (Fig. 2). Efficient slowing

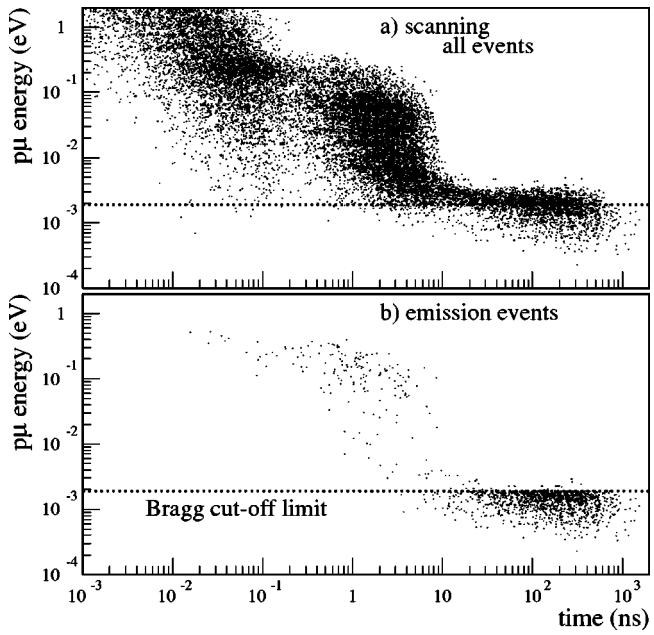

FIG. 4. Slowing down of $p\mu$ atoms in a solid hydrogen layer of thickness 3.4 mg cm^{-2} (1000 Torr l, as defined in Sec. III A). The top plot (a) shows the time and energy after each scattering event during the whole slowing down process. There are 2376 emission events and each $p\mu$ atom undergoes on the average 40 collisions before emission takes place. The bottom plot (b) shows the time and energy for the $p\mu$ atoms which have been emitted from the hydrogen layer. The solid cross sections were used in the simulations.

down finishes after about 10 ns and subsequent $p\mu$ diffusion is determined by elastic Bragg scattering and inelastic phonon scattering. The competition between those two processes is shown in Fig. 6.

The elastic Bragg scattering does not change the $p\mu$ kinetic energy in a solid hydrogen (contrary to a gas, where the elastic scattering is an effective deceleration process because the $p\mu$ atom can always transfer a part of its energy to a recoiling free H_2 molecule). Only inelastic scattering can cause $p\mu$ deceleration (or acceleration from the phonon annihilation process) but is a weak contribution at low energies and at low temperatures. Therefore, $p\mu$ atoms spend a relatively long time in the diffusion stage before reaching the Bragg cutoff energy. In the case of a solid H_2, rapid falloff of the phonon creation cross section at energy E_B makes the $p\mu$ thermalization less deep than in gaseous hydrogen. Indeed, the equilibrium energy defined by the intersection of $\sigma_{11}^{\text{gain}}$ and $\sigma_{11}^{\text{loss}}$ at $\approx$2 meV (see Fig. 2) is still higher than thermal equilibrium in a 3-K gaseous H_2.

The strong increase of the $p\mu(F=0)$ atom mean free path due to the sharp decrease of the cross section below the Bragg cutoff energy is shown in Fig. 7. Such behavior leads to an enhanced emission of cold $p\mu$'s from the thin solid hydrogen layers. We note that a similar phenomenon is used in neutron physics to extract cold neutrons from beams produced in nuclear reactors (polycrystalline filters, see, e.g., Ref. [43]).

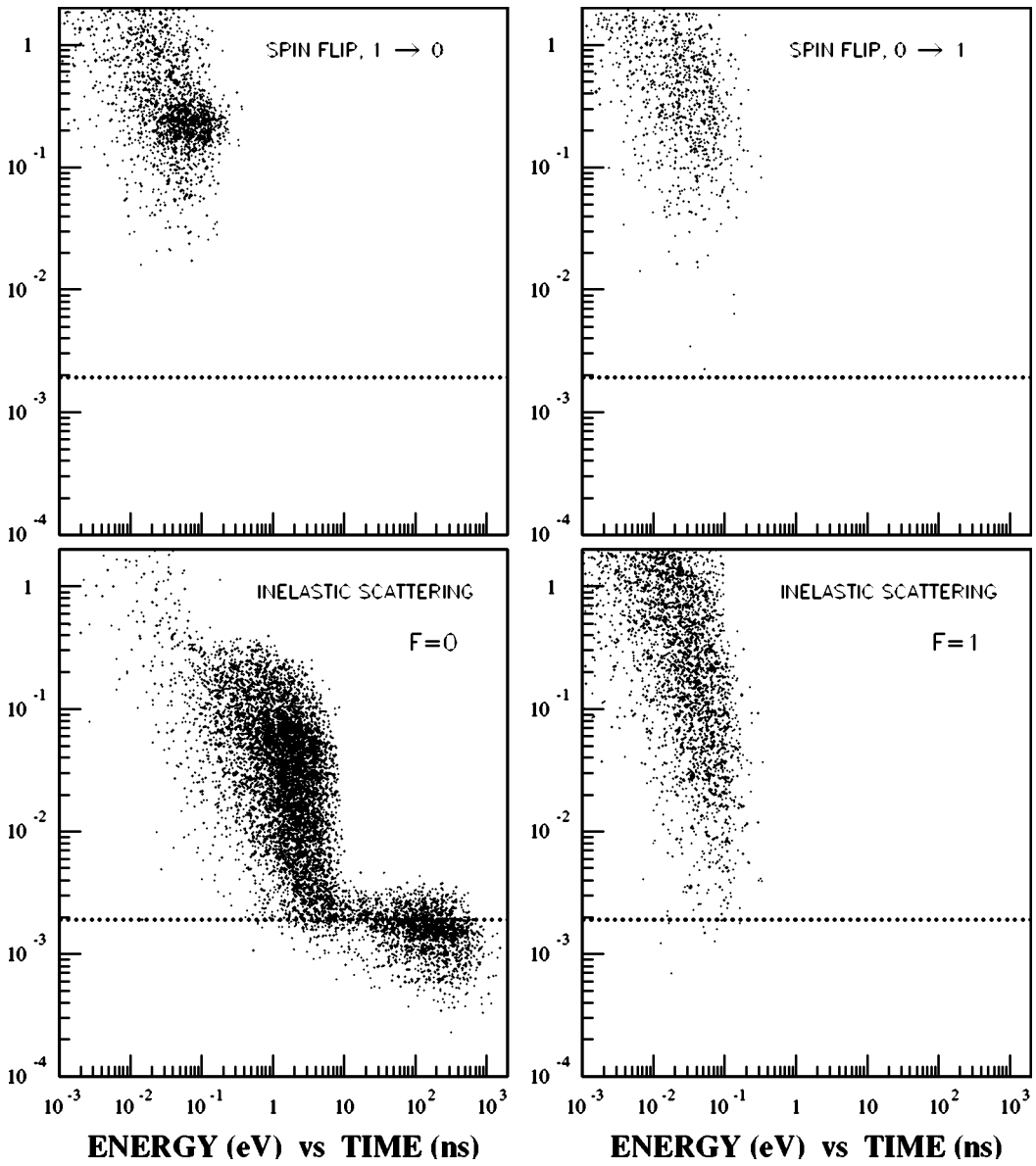

FIG. 5. Details of the scatter plot from Fig. 4(a), namely, the spin-flip contribution (top) and the non-Bragg scattering processes in the slowing down of $p\mu$ atoms (bottom). Note that downward spin flip ($F=1\rightarrow F=0$) increases the energy by $\varepsilon_{hfs}=0.182$ eV and the upward spin flip decreases the energy by that amount. Elastic coherent scattering (not shown in the figure) is a dominant process for energies near the Bragg cutoff energy limit ($\sim 2\times 10^{-2}$ eV) and leaves the energy unchanged.

III. DESCRIPTION OF THE EXPERIMENT

A. The apparatus

The experiments studying $p\mu$ scattering in solid hydrogen were performed at the M20B muon channel at TRIUMF. The layout of the apparatus is shown schematically in Fig. 8. Gaseous hydrogen (or neon) was sprayed, using a special diffusion system, onto the 51-μm-thick gold foil, maintained at 3 K, where it froze creating the thin solid films which could be maintained in high vacuum. The diffuser was inserted from below and could be used to deposit gas on either of the two gold foils separately. The thickness of the film was controlled by adjusting the amount of gas injected. Multilayered targets could be made in which the frozen material consisted of uniform layers, each made from different hydrogen isotopes or other gases such as neon. A versatile gas handling system allowed mixtures of different hydrogen isotopes to be prepared with high precision. The frozen film deposition uniformity, better than 15%, has been measured independently via energy loss of α particles [44]. The amount of gas injected into the system was conveniently measured in units of Torr l, where the conversion factor between Torr l and μg cm^{-2} has been determined [44] and is on average 3.4 μg cm^{-2} per Torr l for H_2. Details of the target construction and working procedure are given in Refs. [18,45]. Details of the data acquisition electronics can be found in Ref. [20]. Incident muons of momentum 26.70 (or 26.25) MeV/c [$\Delta p/p=0.07$ full width at half maximum (FWHM)] were detected by a 127-μm scintillator (1) before traversing a 25-μm-stainless-steel vacuum isolation window. The muons

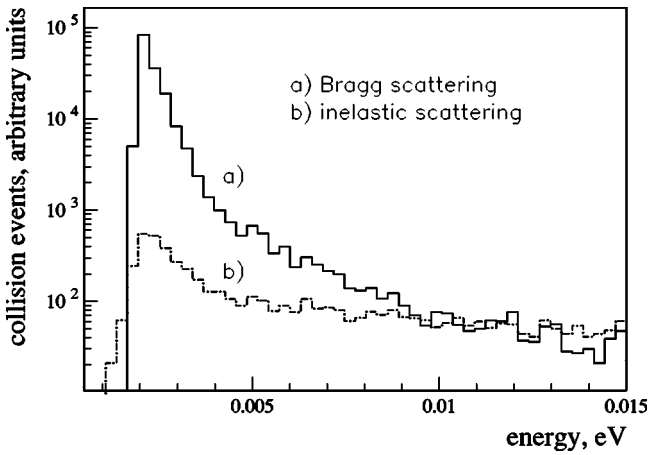

FIG. 6. Competition between Bragg scattering (a) and non-Bragg scattering (b) in $p\mu$ collisions in solid hydrogen for low energies. Note the logarithmic scales.

continued to lose energy while passing through the cryostat 70-K heat shield to eventually stop either in the gold target support foil (2) or in the $\approx$400–800 μm thick solid hydrogen target where they finally formed muonic atoms. The hydrogen target frozen on foil (2), which was placed perpendicularly to the muon beam axis, was called the upstream target (US), and was made of pure protium or of protium with a small admixture of deuterium (or tritium), depending on the experiment (see Figs. 9 and 10).

In the case of a pure protium US target, a thin neon layer was additionally deposited on top, as represented in Fig. 9. In other cases, when deuterium or tritium were present in the US target, we used an additional downstream target (DS) frozen on a second gold foil placed parallel to the first foil but 17.9 mm further along the beam axis [(3) in Fig. 8]. Such an arrangement is presented in Fig. 10, where a thin layer of neon is shown sandwiched between a layer of pure protium

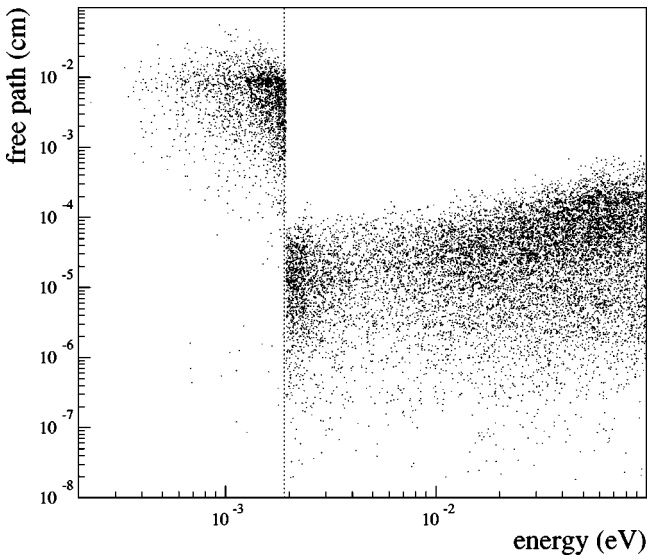

FIG. 7. Sampled values of the $p\mu$ atom mean free path between consecutive collisions vs the collision energy. A strong increase of the mean free path is seen below the Bragg cutoff energy.

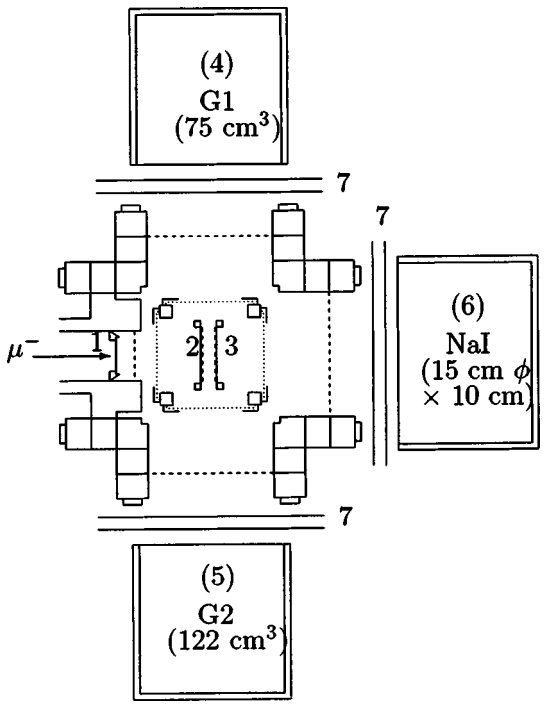

FIG. 8. The apparatus layout showing the muon entrance scintillator (1), the upstream (2), and downstream (3) gold foils (themselves inside the cryostat). The surrounding detectors were the germanium detectors G1 (4) and G2 (5), the NaI (6), and the three pairs of electron counters (7). The drawing is not strictly to scale.

and the DS gold foil, and was used for the TOF studies of the Ramsauer-Townsend effect. A low muon beam momentum was chosen to minimize the number of μ stops in the DS protium layer.

Neon was used to detect the scattered muonic atoms which left the hydrogen layer and subsequently transferred the muon to the neon. The resulting emission of 207-keV x rays from the $2p$-$1s$ μNe transition was observed by two $\sim$100-cm^3 germanium crystals (G1 and G2, Fig. 8) with a time resolution of 10-12 ns (FWHM). The G1 detector was used during the whole experiment, during both the deuterium and the tritium measurements. However, there were two physically different G2 detectors, one for each of the deute-

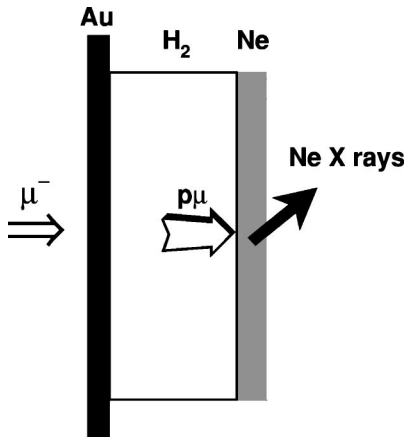

FIG. 9. Single target scheme.

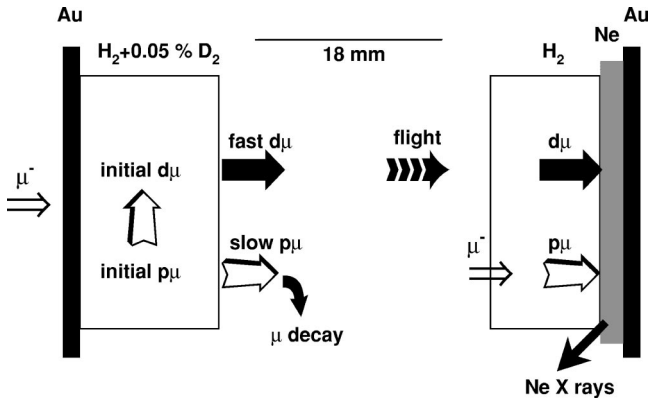

FIG. 10. Double target TOF scheme for $d\mu$. Fast and slow $d\mu$ atoms were emitted forward into the vacuum gap. Although not shown in the drawing, muonic atoms were also emitted toward the gold foils, which we refer to as backward emission.

rium and tritium measurements. The plastic scintillators [(7) in Fig. 8] were located around the target to detect the muon decay electrons. The NaI detector was used to study μCF in hydrogen and deuterium mixtures [25,46].

B. The method

Following muon capture and $p\mu$ formation, the $p\mu$ atoms slow down and diffuse in the hydrogen layer, with some significant fraction of the $p\mu$ atoms escaping the layer. Analyzing the emission yield and the time distribution of the escaped $p\mu$'s gives information about the scattering cross sections. The essential part of the analysis is the comparison of the experimental yields and time distributions with the ones calculated by Monte Carlo (MC). The measurements were performed in two different ways; either by using the single pure protium target covered with a Ne layer (Fig. 9) or by using the parallel target scheme (Fig. 10).

The first method (Fig. 9) proved better for studying $p\mu$ scattering for two reasons: (1) high stopping rate in the US target assured high $p\mu$ emission statistics and (2) the time spectrum was ''clean'' in that it did not contain the overlapping RT part. Table I summarizes the different measurements performed for the study of the RT effect and $p\mu+p$ scattering.

In the second case (Fig. 10), the US target was composed of protium with a small concentration of D_2 (or T_2), which served as a source of energetic $d\mu$ $(t\mu)$ atoms emitted from the layer into the adjacent vacuum with a mean energy of 3.5 eV (9 eV in the case of H_2/T_2 mixture) as a result of the RT effect. Due to the low deuterium (tritium) concentration, $p\mu$'s were predominantly formed as a result of muon stops in the US layer. A small fraction of them survived their evolution in the US hydrogen (no muon transfer to the heavier hydrogen isotope, no $pp\mu$ formation, or muon decay) and left the solid layer after multiple scattering. However, they were very slow ($\varepsilon\approx$ meV) and could not reach the downstream target before the muon decayed. In most cases the muon was transferred from $p\mu$ to a deuterium (tritium) atom. At formation, the muonic deuterium and tritium atoms had a relatively high kinetic energy, about 45 eV, which they subsequently lost in elastic collisions, mainly with protium, until the energy reached the range of the RT minimum in the scattering cross section $\sigma(\mu d+H_2)$. Then the mean distance between collisions increased and the hydrogen layer became effectively transparent for the $d\mu$ $(t\mu)$ atoms which were

TABLE I. Different measurements performed for the RT and $p\mu$ diffusion (diff) studies. 1500 Torr l ($H_2+0.05\%$ D_2) covered with 500-Torr l H_2. DE (deuterium emission). TE (tritium emission)—2000 Torr l ($H_2+0.12\%$ T_2). STE (small tritium emission)—1000 Torr l ($H_2+0.12\%$ T_2). PP (pure protium)—2000 Torr l H_2. SPP (small pure protium)—1000 Torr l H_2. GMU—good muons: i.e., events when only one muon entered the apparatus (no pileup). Conversion factor (for hydrogen): 1 Torr l corresponds to 3.4 μg cm^{-2} for H_2.

Label	Experimental purpose	Beam (MeV/c)	US hydrogen (Torr l)	US neon (Torr l)	DS protium (Torr l)	DS neon (Torr l)	GMU (units of 10^6)
D1	RT	26.70	DE			100	326.9
D2	RT	26.70	DE			50	183.3
D3	RT, diff	26.70	DE		300	50	521.8
D4	RT, diff [a]	26.70	DE		600	50	433.2
D5	diff	26.70	DE	100			96.6
D6	diff	26.70	DE	50			136.9
D7	diff	26.70	PP		300	50	149.4
T1	RT	26.25	TE			30	113.5
T2	RT	26.25	TE			50	174.2
T3	RT, diff [a]	26.25	TE		350	50	405.3
T4	RT, diff	26.25	STE		500	50	147.1
T5	diff	26.25	SPP	10			199.3
T6	diff	26.25	SPP	20			195.8

[a]D4 and T3 are not useful for the $p\mu$ diffusion analysis due to the strong overlap between RT and diffusion parts of the time spectra.

then easily emitted from the solid into the adjacent vacuum. Such energetic emitted muonic atoms traveled through vacuum toward the downstream hydrogen layer and a fraction passed, after possible interactions in hydrogen, to the Ne layer and produced x rays as a result of the muon transfer to neon and subsequent muonic neon deexcitation. Such $d\mu$ ($t\mu$) atoms gave a characteristic peak in the TOF spectrum at ≈ 1 μs—a time determined by the distance between the foils and the position in energy of the Ramsauer-Townsend minimum.

Clearly, not all muons were stopped in the US target and thus those which reached the second foil created $p\mu$'s in the DS protium. The $p\mu$'s diffused to neon giving a contribution to the time spectrum at early times. Thus the resulting Ne time spectrum contained two relatively distinct components, one of them connected with the RT effect in $d\mu$ ($t\mu$) scattering and the other with the diffusion of $p\mu$ atoms in the solid hydrogen. Despite the overlap of the two effects in the time spectra one should note that there is an important advantage of such an experiment. Since the kinetic energy of the $d\mu$ ($t\mu$) is relatively high, the delayed RT peak is not sensitive to the state of the target material and can be well described using either gas or solid scattering cross sections (see Refs. [25,26]). Due to this, the RT peak can be used as a reference in the analysis of the diffusion part where the effects of the solid state can be found.

C. Monte Carlo simulations

The Monte Carlo code FOW [42] was used in the planning stages of the experiment as well as for the analysis to simulate all physical processes occurring after muons pass through the entrance window of the apparatus. Muon stopping distributions along the beam axis in the different apparatus components, especially in the hydrogen layers of the target, have been taken from a special set of measurements [25] and from another Monte Carlo calculation [47] and used as an input to FOW. The FOW code gives the possibility of a full three-dimensional description of the target geometry.

The muonic processes considered are as follows.

(i) Elastic scattering: $p\mu+p$, $p\mu+d$, $d\mu+p$, $p\mu+t$, $t\mu+p$, $d\mu+d$, $t\mu+t$.

(ii) Spin flip: $p\mu(F)\rightarrow p\mu(F')$, $d\mu(F)\rightarrow d\mu(F')$, $t\mu(F)\rightarrow t\mu(F')$.

(iii) Charge transfer: $p\mu\rightarrow d\mu$, $p\mu\rightarrow t\mu$.

(iv) Molecular formation: $p\mu+p\rightarrow pp\mu$, $d\mu+d\rightarrow dd\mu$, $t\mu+t\rightarrow tt\mu$, $d\mu+p\rightarrow pd\mu$, $t\mu+p\rightarrow pt\mu$.

Energy-dependent values of the total and differential cross sections for the elastic scattering of muonic atoms, spin flip, and charge transfer transitions were used in the calculations. For small collision energies (usually below 0.1 eV) the solid double differential cross sections [48] were used for the elastic scattering and spin-flip interactions. At higher energies, where the solid state effects become negligible, the total and single differential gas cross sections from Refs. [9,10,41,49], corrected for molecular effects via the Sachs-Teller model, were applied. Using gas cross sections at higher energies saved computer time without incurring any loss in accuracy. The energy-dependent $pd\mu$, $pt\mu$, and $dd\mu$ (resonant and nonresonant) formation rates were taken from the Faifman calculations [50–52]. The $pp\mu$ and $tt\mu$ formation rates were considered as energy independent ($\lambda_{pp\mu}=3.21$ μs^{-1} [19], $\lambda_{tt\mu}=1.80$ μs^{-1} [53]). Thermal motion of the target molecules was also taken into account. Tables II and III show the main characteristics calculated for different upstream and downstream targets used for $p\mu$ emission study. The values are based on at least 10^6 simulated muons, so the statistical uncertainty is negligible.

TABLE II. Characteristics of the muonic processes in different upstream targets (see column 4 of Table I for target details) as calculated by the Monte Carlo. Muon stops in the targets are given in percent of muons entering the apparatus (the Monte Carlo analog of GMU). The emission yield, molecular formation, backward escape, and muon decay are given in percent per muon stopped. Simulations were performed using the solid cross sections.

Upstream targets	DE	TE	STE	SPP	PP
μ stops	58.6	47.4	32.3	32.3	58.6
$pp\mu$ formation	34.1	24.3	4.8	77.9	83.8
$pd\mu$ formation	39.7				
$pt\mu$ formation		48.5	35.8		
Muon decay	7.1	6.1	2.8	9.5	10.2
Backward escape	13.0	15.2	31.0	8.1	4.1
Forward $p\mu$ emission	1.8	0.4	0.4	4.5	1.9
Forward $d\mu$ emission	4.3				
Forward $t\mu$ emission		5.5	25.2		

Figure 11 shows the calculated energy spectrum of $p\mu$ atoms emitted from the pure protium (PP) target. A strong solid-state effect is evident both in yield intensity and spectral shapes when comparing the calculations which include or disregard the solid hydrogen structure (solid and dot-dashed lines, respectively). The details of the spectral tail above the Bragg cutoff limit are shown on a log-binned scale in the inset. The kinetic energy spectra for $d\mu$ and $t\mu$ atoms emitted from deuterium emission (DE) and tritium emission (TE) targets, respectively, are shown in Fig. 12 for the solid (solid line) and gas (dashed line) cross sections. The lack of solid-state effects is not surprising given the high energy of the atoms involved. The muonic atom energy applies to atoms which have traveled the 17.9 mm distance between the US and DS layers.

TABLE III. Characteristics of the muonic processes in downstream protium targets (see column 6 of Table I for target name references). Muon stops, $p\mu$ emission and $d\mu$ ($t\mu$) transmission are given in percent of muons passing the entrance window of the apparatus. Simulations are performed using the solid cross sections.

Downstream targets (associated US target)	600 DE	500 STE	350 TE	300 DE
μ stops	7.8	9.3	2.6	4.4
Forward $p\mu$ emission	0.6	0.9	0.4	0.7
$d\mu$ transmission	0.7			0.9
$t\mu$ transmission		1.4	0.9	

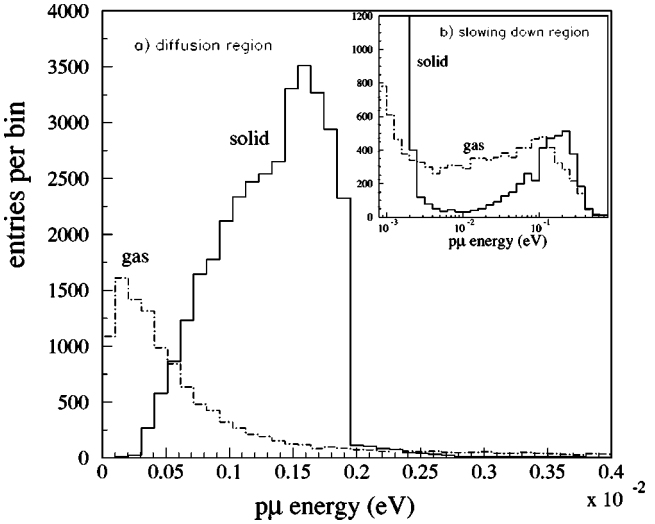

FIG. 11. Calculated low-energy spectrum (a) of emitted $p\mu$ atoms for the PP target. The solid line shows the result using the solid cross sections, whereas the dot-dashed line shows the spectrum using the gas cross sections. The same number of incident muons (2×10^6) is used for both cases. Top-right picture (b) shows the slowing down energy spectrum in a log-binned scale.

Figure 13 shows the probability of $p\mu$ emission from a hydrogen target as a function of the initial $p\mu$ formation position following the muon stop. The example is for the PP target and for the muon stopping distribution for the beam momentum 26.25 MeV/c. The difference between the results of the solid cross sections (solid line) and gas cross sections (dashed line) illustrates the strong increase of the mean free path in the final stage of the $p\mu$ slowing down when the solid-state effects are considered. One can see that the volume from which emitted $p\mu$ atoms can originate is much more extended in the solid case.

IV. MEASUREMENTS

Muonic atom scattering in hydrogen was measured via the x-ray time spectra of μNe $2p$-$1s$ at 207 keV (see Fig. 14).

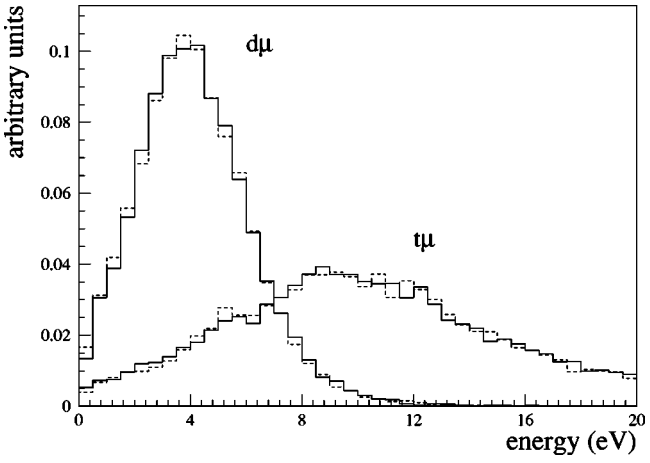

FIG. 12. Energy spectra of $d\mu$ and $t\mu$ atoms emitted from DE and TE targets, respectively, after flying the US-DS distance and before entering the DS target. Solid lines—MC with the solid cross sections, dashed lines—MC with the gas cross sections.

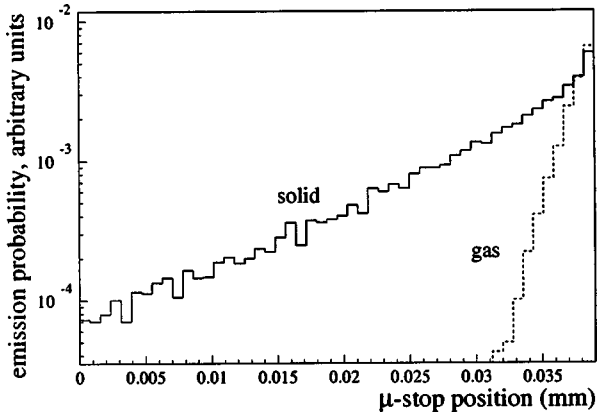

FIG. 13. The probability dependence of $p\mu$ emission from the PP target (for a beam momentum $p=26.25$ MeV/c) vs the initial $p\mu$ position in the target. The simulation was performed using both the solid cross sections (solid line) and gas cross sections (dashed line) for the same number of incident muons.

The time spectra events were selected within the energy window 205.6-208.3 keV. The background time spectra under the 207-keV peak were created using time spectra from two neighboring energy windows, namely, a left background at 203.3–205.6 keV and a right background at 208.3–210.2 keV. Two different background evaluation procedures were used. In the first, the left and right spectra were added, and then normalized by the energy window widths and the resulting spectrum subtracted from the time spectrum of the μNe $2p$-$1s$ peak. The second relied on a multiparameter fit of the summed left and right backgrounds using two exponential functions (with lifetimes for muons in gold and neon) and the background predicted from the fit function was subtracted from the μNe $2p$-$1s$ peak. Since the background accounts for 70%–85% of the total statistics, its removal plays an important role, especially for data at early times where the muon prompt capture in the neon layer and the gold foils bring a strong contribution. Another data cleaning method resulting in better signal to background was the requirement that the muon decay electron be seen *after* the

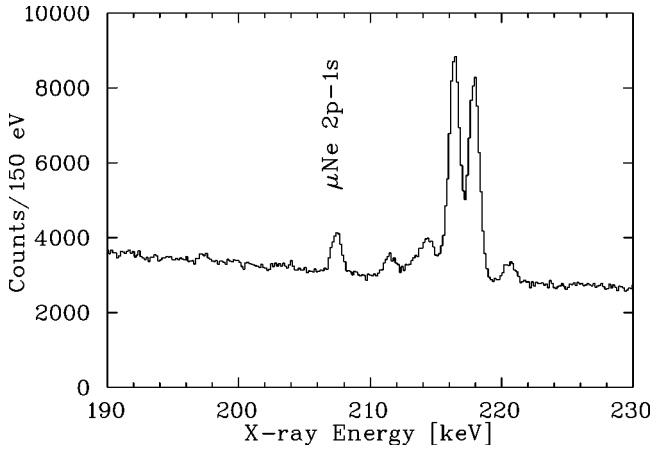

FIG. 14. x-ray energy spectrum for the T3 measurement. The μNe $2p$-$1s$ is located at 207 keV, whereas the bigger peaks around 215–220 keV are the μAu 6–5 lines.

TABLE IV. Experiments for the $p\mu+p$ scattering study. When the hydrogen layer had the same thickness, the different measurements were summed to give more statistics. The last column indicates the signals present in the time spectrum.

No.	Label	Hydrogen (Torr l)	GMU (units of 10^6)	Time spectrum
1	D3+D7	300 DS	671	$p\mu+$ delayed $d\mu$ from DE
2	T4	500 DS	147	$p\mu+$ delayed $t\mu$ from STE
3	T5+T6	1000 US	395	$p\mu$ clean spectrum
4	D5+D6	2000 US	233	$p\mu+d\mu$ diffusion from DE

μNe $2p$-$1s$ x ray, starting from a given time delay. Those delayed electrons were detected by the scintillators (see Fig. 8) during a time interval 0.2–5.2 μs after the μNe signal. This method, called the "del-*e*" criterion, suppressed the background by a factor of about 300. However, useful statistics were reduced by about a factor 10.

A. Combined measurements with H/D and H/T targets

For the $p\mu$ scattering analysis only the few experiments from Table I in which the $p\mu$ diffusion time spectrum have been seen are useful. Similar runs were summed whenever possible and Table IV gives the details. The other measurements were, nevertheless, necessary for the determination of detection efficiencies.

A typical TOF measurement (No. 1, Table IV), where both $d\mu$'s from the US layer and $p\mu$'s from the DS protium layer were detected when they reach the DS neon, is presented in Fig. 15 (points with error bars). The (a) and (b) graphs show the time spectra for the full statistics and for the events where the del-*e* criterion has been applied for background suppression, respectively. That measurement was performed with a DE upstream target (with 0.05% D_2) and a 300-Torr l (H_2) downstream layer. The events occurring at early times ($t<600$ ns) are due to $p\mu$ formed directly in the DS hydrogen which then diffuse to the neon layer. The peak in the TOF spectrum corresponds to the delayed $d\mu$ atoms which travel the distance between the two foils and are not stopped in the DS hydrogen due to the RT effect. Also plotted are the simulations using the solid scattering cross sections as well as the result of the calculation when one neglects the solid-state effects and uses only the gas cross sections.

Another example of a similar TOF measurement (with a hydrogen/tritium mixture in the target upstream and 500-Torr l protium covering the downstream Ne, No. 2) is shown in Fig. 16 for the full statistics and del-*e* requirement cases. A relatively high muon stopping fraction in the downstream target (because the US target was only 1000 Torr l and 9.3% of the muons stopped in the DS target) gives good statistics for the $p\mu$ part in the time spectrum. The delayed peak from $t\mu$ transfer events lies earlier in time than the corresponding deuterium case because of the higher $t\mu$ energy (see Fig. 12), and hence the overlap of both diffusion and RT spectra parts is fairly strong. The solid cross section MC spectrum is also presented in the figure (solid line histogram). Dot-dashed and dotted lines show the predicted contributions from $p\mu$ and $t\mu$, respectively.

Figure 17 shows the time spectrum of $p\mu$ and $d\mu$ atoms emitted together from a DE target (No. 4, Table IV). This case was analyzed using the different emission time dependences since the $d\mu$ part of the time spectrum decreases much faster than the $p\mu$ emission spectrum; the mean diffusion time of dμ in the 2000-Torr l target is $\sim$100 ns, much less than for the $p\mu$ emission ($\sim$300 ns). The $d\mu$ contribution can be removed using the MC simulations since $d\mu$ emission is independent of solid-state effects as one can see from Fig. 15. The subtraction leaves a clean $p\mu$ spectrum which can be compared to the MC including solid-state effects. Normalization of the simulated time spectra was done using the RT peak which is equally well described by both the solid and gas approaches.

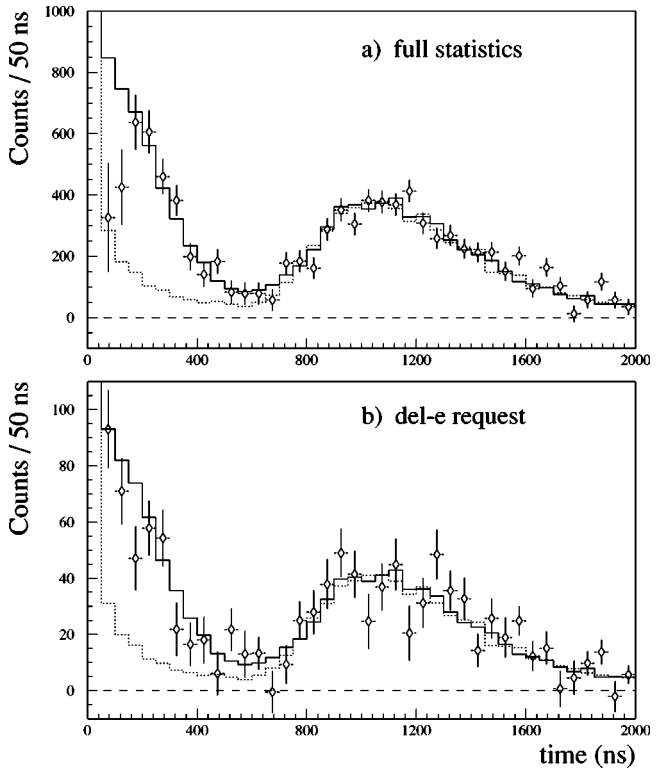

FIG. 15. Experimental time-of-flight spectra (points with error bars) for experiment No. 1 (see Table IV) for cases: (a) full statistics, (b) del-*e* criteria. The solid line represents the Monte Carlo simulation based on the scattering cross sections when solid effects were taken into account, the dotted line is for the gas cross sections.

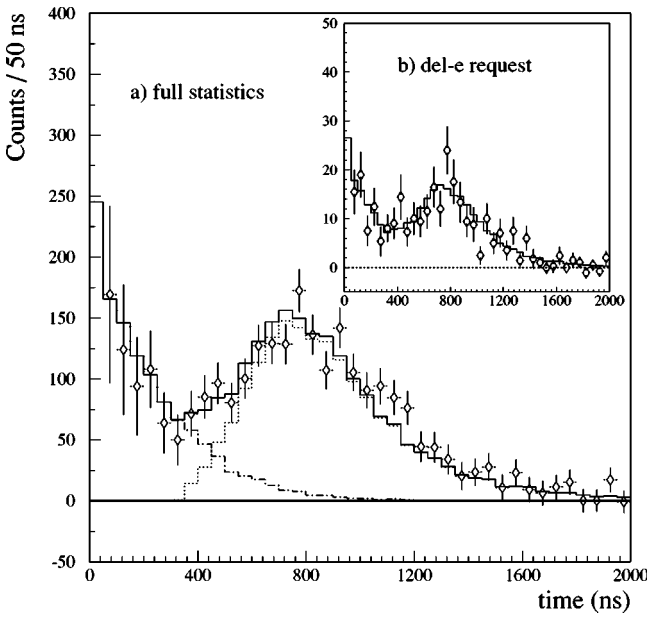

FIG. 16. Experimental time-of-flight spectra (points with error bars) for experiment No. 2 (see Table IV) for (a) full statistics and (b) del-*e* statistics. The solid line is the MC simulation based on the scattering cross sections when solid-state effects were taken into account. Dot-dashed and dotted lines show the $p\mu$ and $t\mu$ contributions, respectively.

The normalization factor $n_{DS}=Y_{expt.}/Y_{MC}$, where the yields $Y_{expt.}$ and Y_{MC} were the total counts in the time interval 500–2500 ns, was calculated from all eight measurements given in Table I which deal with the RT effect. The mean weighted value for the germanium detector G1 (which was the same in all experimental runs) was $n_{DS}=(5.8\pm0.3)\times10^{-4}$. This normalization factor is, in effect, the detector efficiency for Ne x rays detected from the DS neon layer. For experiment Nos. 3 and 4 (see Table IV) where x rays were detected from neon on the US target (shifted by 17.9 mm compared to the DS target) another method was used to determine the normalization coefficient. Because there are no RT peaks in those time spectra of Ne x ray, a direct comparison between experiment and MC cannot be used. However, the efficiency to detect DS Ne x rays was the same for prompt events and for events delayed by diffusion. We determined the experimental ratio between US prompt Ne x rays and DS prompt Ne x rays, using D1 and D5 experiments, where the Ne layer thickness was the same, just shifted in location. By multiplying that ratio with the previous DS efficiency n_{DS} we obtained the G1 detector US MC normalization coefficient $n_{US}=(8.1\pm1.0)\times10^{-4}$, $\approx40\%$ higher than in the DS case, with an error which takes into account the statistical errors of both measurements as well as the n_{DS} error. No efficiency was determined for the G2 germanium detector, because it was changed between the deuterium and tritium measurements.

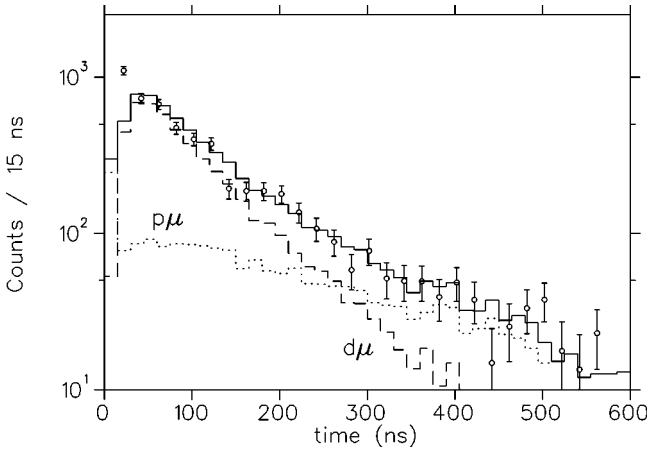

FIG. 17. Experimental time spectrum (points with error bars) of $p\mu$ and dμ emitted together from DE upstream target (experiment No. 4, Table IV). Monte Carlo simulation is shown as the solid line histogram. Dotted and dashed curves show the contributions from $p\mu$ and $d\mu$, respectively. Calculations based on solid cross sections.

B. Emission of $p\mu$ atoms from a layer of solid hydrogen

Although $p\mu$ atom emission was a parasitic process in the RT experiments, those runs were still useful for the analysis of $p\mu$ scattering in solid hydrogen. In particular, the profound disagreement between experimental data and theory using gas cross sections and the relative correctness of the solid cross sections can be seen.

The observation of enhanced $p\mu$ emission from solid hydrogen stimulated additional measurements specifically intended to study the phenomenon more precisely with higher statistics. A target similar to the one shown in Fig. 9 was made from 1000-Torr l pure protium covered with a thin (10–20 Torr l) neon layer. The resulting time spectrum of μNe $2p$-1s x rays described the diffusion of $p\mu$ atoms in hydrogen from the moment of the muon stop to the moment of emission.

The measured time spectra (No. 3, Table IV) of μNe $2p$-1s x rays are shown in Fig. 18 for the full statistics and del-*e* criteria. MC spectra also shown in the figures describe well the experimental data when the solid cross sections are used (solid lines). Normalization to the experimental data is based on the conclusions from the TOF measurements (see Sec. IV A). The calculation with the gas cross sections (dotted lines) gives a suppressed yield although the lifetimes representing the diffusion are not dramatically different.

V. ANALYSIS AND DISCUSSION

As is seen from the comparison between the experimental results and the simulations performed using both the solid and gas cross sections presented on Fig. 15, both types of cross section describe the RT part of the spectrum equally well. That agreement is due to the fact that solid-state effects are negligible for the energies of the $d\mu$ atoms which are responsible for those spectra. A similar conclusion can be drawn from the measurements with $t\mu$.

In contrast, there is a big difference in yields as well as in time dependence between the calculated $p\mu$ diffusion spectra and measurements where an agreement with the experi-

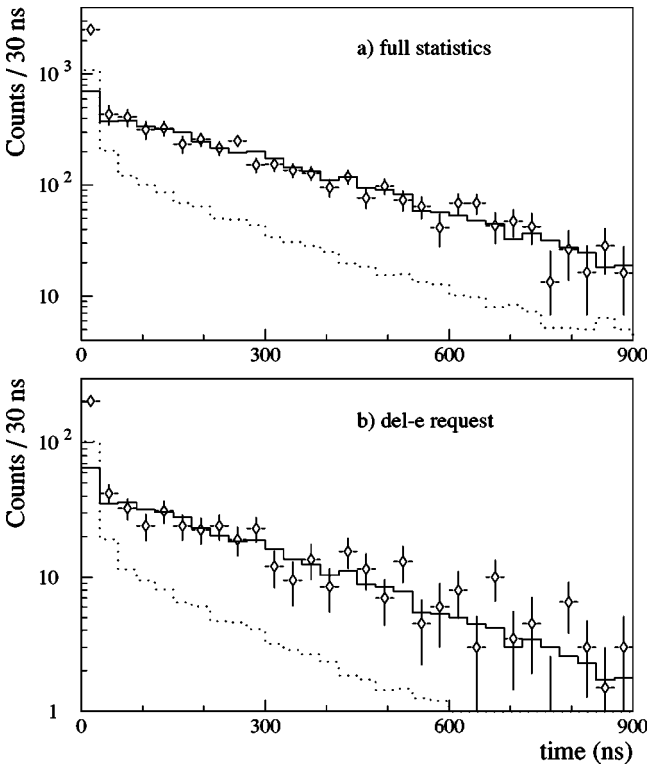

FIG. 18. Experimental (points with error bars) and MC (lines) time spectra of $p\mu$ emitted from the 1000-Torr l H_2 layer (No. 3, Table IV) for the full experimental statistics (a), and del-*e* criteria (b). Solid line—calculation with the solid cross sections; dotted line—calculation for the gas cross sections. Calculations with solid cross sections are normalized to the experimental data according to conclusions from the TOF measurements.

ment is obtained only for the solid cross sections; the discrepancy seen in Fig. 15(a) for first points from times 0–150 ns has an artificial source and will be explained later in this section. The gas cross sections predict a total yield of emitted $p\mu$'s two times smaller than required for a correct description of the experimental results. If one excludes the first channel (Fig. 15), which contains events connected with fast $p\mu$ atoms from the slowing down stage, the gas approach gives three times less emission.

The good agreement between experiment and calculation based on the solid cross sections is also visible in Fig. 16 where the emission spectrum of $p\mu$'s from the DS target and the transmission spectrum of the delayed $t\mu$'s from the small tritium emission US target are presented. The $p\mu$ emission is enhanced 2.3 times for the total emission and 3.8 times for emission at times $t>30$ ns. Accurate results, especially from the point of view of the emitted $p\mu$ diffusion time analysis, are obtained from the experiment with the small pure protium target (Fig. 18). In that case there were no ambiguities between signals from diffusion and those from RT events, which was a problem present in the measurements with the combined H/D and H/T targets. However, such combined target measurements were necessary because they gave the RT peak which was used as the reference for the yield normalization of the MC spectra. The time distribution of the emitted $p\mu$ atoms has some nontrivial behavior and depends

TABLE V. Diffusion time of $p\mu$ atoms, τ_d in ns, in solid hydrogen layers of different thicknesses (No.'s defined in Table IV).

No.	Target (Torr l)	Experiment		MC	
		Full statistics	Del-*e*	Solid	Gas
1	300	161(32)	183(35)	141(4)	257(26)
2	500	199(40)	360(165)	222(7)	234(14)
3	1000	269(13)	279(44)	258(3)	237(8)
4	2000	279(26)	253(42)	254(8)	230(24)

[a]statistical error is used for the fit

not only on the cross sections but also on the target thickness, the muon stop distribution in the target, and the initial energy of the $p\mu$ atoms. In the limit of long times and for a given μ-stop distribution, the $p\mu$ emission time distribution can be well modeled by a one-exponential approximation. In that limit, the constant factor in the exponent represents the mean time needed for the equilibrated $p\mu$ atoms to reach the layer boundary (we call that parameter the diffusion time, τ_d). Such a τ_d depends on the target thickness but should reach an asymptotic value for high thickness simply because the μ-stop distribution is effectively modeled by exponential decreasing as a function of thickness (cf. Fig. 1 of Ref. [42]). When convoluted with the escape probability of Fig. 13, and the associated escape time from any given depth, this exponential behavior of the stopping yields a constant emission time. In light of the remarks presented above, we chose a unique time region $t>200$ ns for the analysis of the four experimental time spectra (see Table IV) to determine the diffusion time τ_d and compare it with the MC simulation.

Such a choice had the additional advantage that it avoided problems with the early parts of the time spectrum. The problem is clearly visible in Fig. 15(a) for times less than 200 ns in a measurement made with a thick US layer plus a H_2 DS layer. The early time signal was only a few percent of the total counts so the background subtraction for those time regions was significant, as can be seen from the resulting uncertainties, and hence any small irregularities in the thresholds and in the detection of secondary muons as well as in the background estimation itself can result in an poor estimation of the background. It also exists, but is less important, in measurements with a H_2 US layer, where the percentage of incident muons stopped US was significantly higher than in the downstream layer. It is worth noting that for the spectra cleaned with the del-*e* condition, where all the background problems vanish, the theory (via Monte Carlo simulations) agrees with the early time region, but a more sophisticated analysis was not possible because of poor statistics and the complicated form of the time spectra.

The measured and calculated values of τ_d, fitted using a single-exponential distribution, are given in Table V for both data treatments (i.e., with and without del-*e*). Good agreement between the experimental values of τ_d and the calculations using the solid cross sections is observed for each experiment. The results are also shown in Fig. 19 where the points with error bars represent the experimental values of τ_d from Table V. The lines are the results from the Monte Carlo

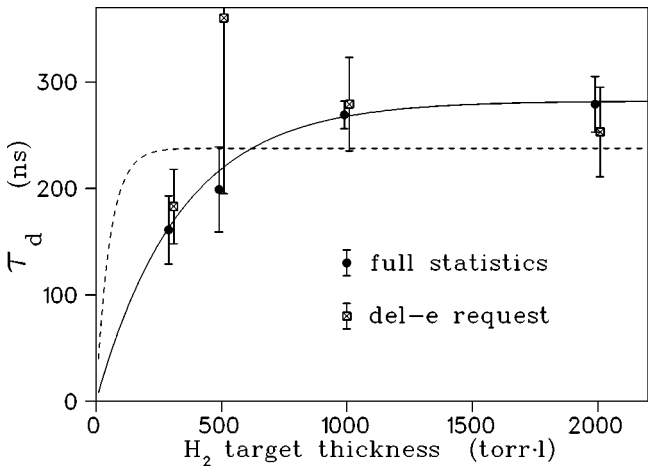

FIG. 19. The dependence of the diffusion time τ_d on H_2 layer thickness. Solid and dashed lines were calculations using solid and gas cross sections, respectively.

calculations using the solid and gas cross sections (solid and dotted lines, respectively). The MC results from Table V were obtained strictly for the given experimental conditions whereas the calculations represented by the continuous lines in Fig. 19 were made assuming pure protium layers of increasing thickness and using the same muon stopping distribution (beam momentum of 26.25 MeV/*c*) in order to show the smooth dependence of τ_d on the target thickness.

The analysis of the emission yields of the slow $p\mu$ atoms supports also the use of the solid cross sections. This is seen by comparing the experimental results with the simulations when the solid and gas cross sections were used. The results for the G1 detector are presented in Table VI. The comparison was performed for the time interval 200–600 ns, characteristic for the diffusion process, using the efficiencies established from the RT time domain (see Sec. IV A). The agreement between the experiments and solid cross sections is excellent.

Despite the general agreement between the experimental data and the theoretical description of $p\mu$ diffusion in fully modeled solid hydrogen, the question of the sensitivity of the calculated diffusion time and emission yield on the cross sections is important. The influence of an inaccuracy in the

TABLE VI. Comparison of the calculated and measured (full statistics) $p\mu$ atom emission yields (in percent per GMU) from the different solid hydrogen layers for the time interval 200–600 ns. The second column represents the total hydrogen thickness in both US and DS.

No.	Hydrogen thickness (Torr l)	Experiment	MC[a]	
			Solid	Gas
1	2000+300	0.21(2)	0.225(5)	0.059(2)
2	1000+500	0.35(6)	0.345(6)	0.067(3)
3	1000	0.52(7)	0.521(7)	0.313(6)
4	2000	0.38(6)	0.398(6)	0.074(3)

[a]Only the statistical error is given.

$p\mu+D_2$ (T_2) and $d\mu(t\mu)+X$ (X is any hydrogen isotope) cross sections is negligible in the $p\mu$ diffusion study because of the very small concentration of deuterium (tritium) admixtures in the targets. The question of $d\mu+H_2$, $t\mu+H_2$ cross sections in the Ramsauer-Townsend region is discussed elsewhere [25,26].

To study the sensitivity of the $p\mu+H_2$ scattering simulation on the cross sections we performed calculations with the solid scattering cross sections scaled in the low-energy region (i.e., collision energy <0.1 eV). When applying a constant scaling factor, between 0.7 and 1.3, it only changes the character of the slowing down process by a very small amount at short times. However, it does not change the diffusion process in any practical way. Variations in the diffusion time τ_d and the total emission yield do not exceed 0.5%–1% for the mentioned scaling range. This is not surprising since the scaling does not change the characteristic equilibrium energy of the diffused $p\mu$ which is established by the deceleration and acceleration processes (i.e., creation and annihilations of phonons, respectively). That energy is close to the Bragg cutoff energy E_B, because the coherent phonon creation for $p\mu(F=0)$ vanishes below E_B (a weak incoherent scattering remains) and the inelastic-scattering cross sections for the acceleration (σ_{11}^{gain}) and deceleration (σ_{11}^{loss}) cross over near E_B (Fig. 2). Following these remarks, the value of E_B may have an influence on the cold $p\mu$ emission (but not on the diffusion time). However, the E_B value is defined by the geometrical structure of the hydrogen crystal (lattice constant) and thus is known relatively precisely (better than 5%). One result of the simulations was that such a 5% shift of E_B (0.1 meV) gives an increase (or decrease) of the $p\mu$ emission yield by 1.2%.

Another important factor which can influence the $p\mu$ diffusion parameters is the $pp\mu$ molecular formation rate, which is the most frequent $p\mu$ disappearance channel following muon decay. Both parameters—the diffusion time τ_d and the emission yield, Y—are sensitive to that process. The value $\lambda_{pp\mu}=3.21\pm0.18\ \mu s^{-1}$ [19] used in our simulations is the more accurate value of the two existing measurements performed in solid hydrogen to date. Decreasing $\lambda_{pp\mu}$ by one standard deviation resulted in a 4% increase of the calculated diffusion time and a similar increase of the emission yield from a thick hydrogen layer. Nevertheless, when one takes into account all above systematic errors, the comparison presented in Tables V and VI allows us to conclude that theory based on the solid cross section is still consistent with the experimental results, contrary to that of the gas approach.

In this work we tried to confront the experimental results obtained for $p\mu$ atom scattering in solid hydrogen with the theory of low-energy scattering including solid state effects. Agreement has been obtained between experiment and that theory with respect to $p\mu$ diffusion. In particular, the diffusion time has been found and the enhanced yield of $p\mu$ emission from the thin solid hydrogen layers has been explained. The results of the study proved that the observed solid effects in the scattering at low energies (collision energy <0.1 eV) are correctly described by the calculated solid scattering cross sections. The experimentally observed

enhancement in the emission of cold $p\mu$ atoms creates the possibility of using such neutral atomic beams as a tool in further studies of muonic processes.

ACKNOWLEDGMENTS

The authors would like to thank V. E. Markushin, J. L. Douglas, and M. Maier for fruitful discussions and for their help during the data acquisition period. This work is supported by the Polish Committee for Scientific Research, the Swiss National Science Foundation, the Natural Sciences and Engineering Research Council of Canada, TRIUMF, the Russian Foundation for Basic Research (Grant No. 01–02–16483), and the NATO Linkage Grant No. LG9301162.

[1] W.H. Breunlich, P. Kammel, J.S. Cohen, and M. Leon, Annu. Rev. Nucl. Part. Sci. **39**, 311 (1989).
[2] L.I. Ponomarev, Contemp. Phys. **31**, 219 (1990).
[3] P. Froelich, Adv. Phys. **41**, 405 (1992).
[4] D. Measday, Phys. Rep. **354**, 243 (2001).
[5] V.P. Dzhelepov, P.F. Ermolov, and V.V. Fil'chenkov, Zh. Eksp. Teor. Fiz. **49**, 393 (1965) [Sov. Phys. JETP **22**, 275 (1966)].
[6] A. Bertin, A. Vitale, and A. Placci, Riv. Nuovo Cimento **5**, 423 (1975).
[7] A. Bertin *et al.*, Nuovo Cimento Soc. Ital. Fis., A **72**, 225 (1982).
[8] V.M. Bystritsky *et al.*, Zh. Eksp. Teor. Fiz. **87**, 384 (1984) [Sov. Phys. JETP **60**, 219 (1984)].
[9] L. Bracci *et al.*, Muon Catal. Fusion **4**, 247 (1989).
[10] V.S. Melezhik and J. Woźniak, Muon Catal. Fusion **7**, 203 (1992).
[11] A. Adamczak *et al.*, At. Data Nucl. Data Tables **62**, 255 (1996).
[12] A. Adamczak, Hyperfine Interact. **82**, 91 (1993).
[13] J.S. Cohen, Phys. Rev. A **34**, 2719 (1986).
[14] A. Boukour *et al.*, Phys. Rev. A **53**, 3314 (1996).
[15] V.M. Bystritsky, Nukleonika **40**, 37 (1995).
[16] D.J. Abbott *et al.*, Phys. Rev. A **55**, 214 (1997).
[17] G.M. Marshall *et al.*, Hyperfine Interact. **82**, 529 (1993).
[18] P.E. Knowles *et al.*, Nucl. Instrum. Methods Phys. Res. A **368**, 604 (1996).
[19] F. Mulhauser *et al.*, Phys. Rev. A **53**, 3069 (1996).
[20] P.E. Knowles *et al.*, Phys. Rev. A **56**, 1970 (1997); **57**, 3136(E) (1998).
[21] M.C. Fujiwara *et al.*, Phys. Rev. Lett. **85**, 1642 (2000).
[22] T.A. Porcelli *et al.*, Phys. Rev. Lett. **86**, 3763 (2001).
[23] G. Marshall *et al.*, Hyperfine Interact. **138**, 203 (2001).
[24] R. Jacot-Guillarmod *et al.*, Hyperfine Interact. **101/102**, 239 (1996).
[25] F. Mulhauser *et al.*, Hyperfine Interact. **119**, 35 (1999).
[26] F. Mulhauser *et al.*, Hyperfine Interact. **138**, 41 (2001).
[27] J. Woźniak *et al.*, Hyperfine Interact. **119**, 63 (1999).
[28] V. Bystritsky *et al.*, Hyperfine Interact. **138**, 47 (2001).
[29] A. Adamczak, Hyperfine Interact. **119**, 23 (1999).
[30] S. Gershtein, Zh. Eksp. Teor. Fiz. **34**, 463 (1958) [Sov. Phys. JETP **7**, 318 (1958)].
[31] S.I. Vinitskiĭ and L.I. Ponomarev, Fiz. Elem. Chastits At. Yadra **13**, 1336 (1982) [Sov. J. Part. Nucl. **13**, 557 (1982)].
[32] A.V. Matveenko, L.I. Ponomarev, and M.P. Faifman, Zh. Eksp. Teor. Fiz. **68**, 437 (1973), [Sov. Phys. JETP **41**, 212 (1973)].
[33] L.I. Ponomarev, L.N. Somov, and M.P. Faifman, Yad. Fiz. **29**, 133 (1979), [Sov. J. Nucl. Phys. **29**, 67 (1979)].
[34] M. Bubak and M. P. Faifman, JINR Report No. E4–87–464, 1987 (unpublished).
[35] M. Struense, J. Cohen, and R. Pack, Phys. Rev. A **34**, 3605 (1986).
[36] J.S. Cohen and M.C. Struensee, Phys. Rev. A **43**, 3460 (1991).
[37] V.S. Melezhik, L.I. Ponomarev, and M.P. Faifman, Zh. Eksp. Teor. Fiz. **85**, 434 (1983) [Sov. Phys. JETP **58**, 254 (1983)].
[38] V.S. Melezhik, J. Comput. Phys. **65**, 1 (1986).
[39] I.F. Silvera, Rev. Mod. Phys. **52**, 393 (1980).
[40] P. Souers, *Hydrogen Properties for Fusion Energy* (University of California Press, Berkeley, California, 1986).
[41] C. Chiccoli *et al.*, Muon Catal. Fusion **7**, 87 (1992).
[42] J. Woźniak, V.M. Bystritsky, R. Jacot-Guillarmod, and F. Mulhauser, Hyperfine Interact. **101/102**, 573 (1996).
[43] P.A. Egelstaff, *Thermal Neutron Scattering* (Academic Press, London, 1965).
[44] M.C. Fujiwara *et al.*, Nucl. Instrum. Methods Phys. Res. A **395**, 159 (1997).
[45] G.M. Marshall *et al.*, Hyperfine Interact. **101/102**, 47 (1996).
[46] A. Olin *et al.*, Hyperfine Interact. **118**, 163 (1999).
[47] R. Jacot-Guillarmod, *Stopping Code* (University of Fribourg, Fribourg, 1997).
[48] A. Adamczak, *Cross Sections Data File* (Institute of Nuclear Physics, Cracow, 1997).
[49] V.S. Melezhik and J. Woźniak, Hyperfine Interact. **116**, 17 (1998).
[50] M.P. Faifman, Muon Catal. Fusion **4**, 341 (1989).
[51] M.P. Faifman, Muon Catal. Fusion **2**, 247 (1988).
[52] L.I. Ponomarev and M.P. Faifman, Zh. Eksp. Teor. Fiz. **71**, 1689 (1976) [Sov. Phys. JETP **44**, 886 (1976)].
[53] W.H. Breunlich *et al.*, Muon Catal. Fusion **1**, 67 (1987).